JM3 Journal of Micro/Nanopatterning, Materials, and Metrology

RESEARCH PAPER

Achromatic Talbot lithography with partially coherent extreme ultraviolet radiation: mask and illumination parameter optimization

Bernhard Lüttgenau,[a,b,*] Sascha Brose,[a,b,c] Serhiy Danylyuk,[c] Jochen Stollenwerk,[a,b,c] and Carlo Holly[a,b,c]

[a]RWTH Aachen University, Chair for Technology of Optical Systems, Aachen, Germany
[b]JARA – Fundamentals of Future Information Technology, Jülich, Germany
[c]Fraunhofer Institute for Laser Technology, Aachen, Germany

ABSTRACT. **Background:** Compact extreme ultraviolet (EUV) exposure tools utilizing partially coherent radiation are ideally suited for industrial EUV resist qualification regarding sensitivity, contrast, and resolution. For the broad applicability of the technology, the achievable resolution is crucial and requires thorough investigation.

Aim: The investigation of limiting factors for the achievable resolution for achromatic Talbot lithography is an important step in creating compact EUV exposure tools for industrial resist qualification and high-resolution patterning, accelerating the research and development of high-resolution EUV photoresists for next-generation microchips and processes.

Approach: To maximize the contrast of the resulting intensity distribution in the wafer plane for high-resolution patterns, both the illumination parameters and the utilized transmission masks are investigated by rigorous coupled-wave analysis simulations. The main influencing factors on the achievable resolution are identified and presented. In addition to the simulative optimization of the phase-shifting masks, the fabrication of the dense periodic nanopatterns becomes increasingly challenging for smaller periods. The mask fabrication process is therefore optimized to create stable and high-resolution periodic mask patterns.

Results: Rigorous simulation of the achievable aerial image contrast in the wafer plane demonstrates the influence of partial coherence as well as the geometry and material selection of the mask. For the current mask design, the theoretical resolution is limited to a 14-nm half-pitch (wafer scale). The mask fabrication process is optimized leading to an experimental record resolution of 32.5-nm half-pitch for lines and spaces as well as 28-nm half-pitch for pinhole patterns with the presented demonstrator setup. Metal-based masks with optimized geometry will allow for the fabrication of 6.5-nm half-pitch patterns (wafer scale).

Conclusions: Achromatic Talbot lithography can be used in compact EUV exposure tools with a theoretical resolution below 10-nm half-pitch (wafer scale). The main influencing factors on the achievable resolution are the mask material used and the degree of coherence of the utilized radiation.

© The Authors. Published by SPIE under a Creative Commons Attribution 4.0 International License. Distribution or reproduction of this work in whole or in part requires full attribution of the original publication, including its DOI. [DOI: 10.1117/1.JMM.23.4.043002]

Keywords: laboratory exposure tool; achromatic Talbot lithography; interference lithography; holographic lithography; resist characterization; phase-shifting masks; transmission gratings; aerial image contrast

Paper 24055G received Aug. 6, 2024; revised Oct. 19, 2024; accepted Oct. 21, 2024; published Dec. 18, 2024.

*Address all correspondence to Bernhard Lüttgenau, bernhard.luettgenau@rwth-aachen.de

1 Introduction

Dense periodic nanostructures with feature sizes below 100 nm are essential for numerous industrial and scientific applications, such as photoresist qualification for achieving high resolution[1,2] and the creation of high-resolution structures to produce, e.g., metamaterials, biosensors, quantum dot arrays, and artificial crystals.[3–5] Fabricating these nanostructures is a complex task, requiring advanced patterning technologies such as electron beam lithography, nanoimprint lithography, or industrial projection lithography for structure definition. Each method has its strengths and limitations. Electron beam lithography offers high resolution but suffers from limited throughput. Nanoimprint lithography provides high throughput but lacks pattern fidelity for large-area nanopatterning. Industrial projection lithography ensures high pattern fidelity and throughput, but its application is mostly limited to major companies in the semiconductor industry due to high investment and operational costs. Qualifying next-generation photoresists for extreme ultraviolet (EUV) lithography presents even greater challenges as it often demands resolutions beyond the state of the art. Research on photoresists and related processing relies mostly on high-volume manufacturing (HVM) tools[6] and synchrotron facilities.[7–10] To optimize the photoresist development process and ensure quality control, systematic investigations on the achievable sensitivity, contrast, and resolution are necessary. However, using HVM tools for these tasks is often impractical due to their high operational cost and complexity, so operating such tools at the resist supplier's site is not feasible. Synchrotrons provide spatial and temporal coherent EUV radiation with high intensity and allow for lithographic approaches such as dual-grating interference lithography, leading to the highest demonstrated resolution.[9] Despite their advantages, the limited number of synchrotron facilities and the limited availability of beamtime slow down the corresponding research and development, resulting in a long lead time for new products.

To address these issues, compact nanopatterning tools using EUV radiation are a promising solution. The developed compact EUV exposure tool at Rheinisch-Westfälische Technische Hochschule (RWTH) Aachen University and Fraunhofer Institute for Laser Technology (ILT) employs a discharge-produced plasma (DPP) EUV source[11] for large-area nanopatterning and industrial EUV photoresist qualification.[12] Talbot lithography has proven to be a suited lithographic approach utilizing all diffraction orders from a transmission grating resulting in high-throughput patterning.[13,14] The use of interference results in homogeneous and high-contrast intensity modulations. In addition, achievable pattern demagnification of the mask pattern and an effective local defect compensation are both considered strong advantages of the structuring method.[15,16] In contrast to more advanced interference lithographic methods like dual-grating interference lithography, Talbot lithography allows the usage of both coherent and partially coherent radiation with defined relative spectral bandwidth and moderately low photon flux, making it ideal for both plasma-based EUV radiation sources[15,16] and synchrotrons.[17] The achievable resolution of the nanopatterns can in theory be as low as $\lambda/4$, but in practical applications depends on several factors, including the optical properties of the incident EUV radiation, the stability of the mask-wafer-positioning system, the photoresists performance, and the resolution material choice and quality of a used transmission mask.

The presented study involves a rigorous simulative evaluation of illumination parameters and phase-shifting mask designs for achromatic Talbot lithography at EUV wavelengths. The goal is to improve the resolution, demonstrate sub-30-nm patterning, and formulate guidelines for reaching sub-10-nm resolution (wafer scale). The results pave the way toward a compact EUV exposure setup suitable for both industrial EUV photoresist qualification and large-area nanopatterning for various scientific applications.

2 Achromatic Talbot Lithography

Achromatic Talbot lithography is a lithographic approach that is based on the self-imaging of a grating pattern due to interference of the propagating grating diffraction orders.[18,19] It is suited for coherent to partially coherent radiation and can be utilized for high-resolution nanopatterning of dense periodic structures especially over large areas. The working principle of the (achromatic) Talbot lithography is shown in Fig. 1(a). The EUV radiation is diffracted by the grating structures of the transmission mask and forms a complex intensity modulation behind the mask. The bright

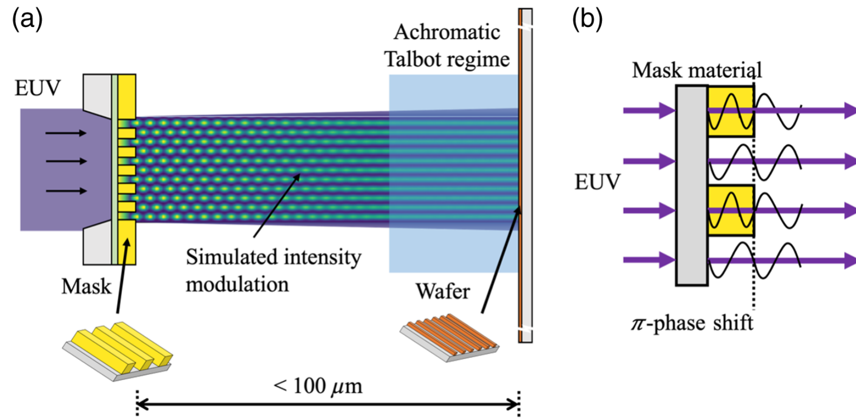

Fig. 1 Principle of Talbot lithography with the achromatic Talbot regime indicated by the blue shaded box near the wafer plane. The bright spots mark the intensity maxima in the interference pattern. In the achromatic Talbot regime, a pattern demagnification by a factor of 2 is achieved for line structures (a). Schematic representation of the working principle of a phase-shifting transmission mask and the definition of the geometrical parameters (b). Picture adapted from Lüttgenau et al.[20]

spots in the intensity distribution mark intensity maxima in the interference pattern (Fig. 1). At defined distances behind the mask, the intensity distribution at the contact point ($z = 0$) is replicated in the aerial image. These Talbot distances can be calculated by $z_{T,n} = n\lambda/\left(1 - \sqrt{1 - \lambda^2/p^2}\right)$ with λ being the wavelength of radiation, p the grating period and n a positive integer.[21] For irradiation with a certain spectral bandwidth $\Delta\lambda$, the intensity maxima of the intensity distribution broaden along the propagation axis (z-axis) with increasing distance from the mask. Above a certain distance behind the mask, the achromatic Talbot distance $z_a = 2p^2/\Delta\lambda$, and the intensity maxima overlap completely and form a stable intensity distribution with two times reduced periodicity with respect to the mask periodicity [indicated by the blue square in Fig. 1(a)]. Due to this effect, achromatic Talbot lithography can be used to enable a two-time pattern demagnification of the mask pattern in the exposure result.[12,17] In addition, the stable behavior of the intensity modulation in the achromatic Talbot regime reduces the precision requirements for mask–wafer positioning and accepts some degree of displacement or tilt.

As the achromatic Talbot lithography approach is perfectly suited for partially coherent radiation with a relative spectral bandwidth of ~2% to 4%, it can be utilized for nanopatterning approaches using radiation from plasma-based EUV sources if operated with an argon/xenon gas mixture resulting in a main wavelength of 10.9 nm.[11,22] If EUV radiation with a main wavelength of 13.5 nm is required, e.g., for photoresist characterization, the source is operated with xenon only, and the emitted radiation is spectrally filtered to the target wavelength and spectral bandwidth by reflection on a tailored multilayer mirror.[23]

The spatial coherence length l_s of the emitted radiation can be defined by the angular extent θ of the source as $l_s = \ln(2)\lambda/\pi \tan(\theta)$. It determines the maximum mask to wafer distance $z_{\max} = l_s p/2\lambda$ at which coherent superposition of the diffraction orders still occurs. Together with the spectral bandwidth, this also determines the depth of the distance window that can be utilized for exposure in the distance regime of achromatic Talbot lithography.[12] For plasma-based EUV sources, the spatial coherence is limited and can only be increased by spatial filtering or by increasing the mask-source distance. As this will lead to a reduced intensity in the wafer plane, the spatial coherence is kept between 20 and 40 μm in practice. This leads to an exposure distance window below 100 μm in which the mask needs to be positioned precisely with respect to the wafer.

For high-resolution patterning within this distance window, the intensity contrast of the aerial image $(I_{\max} - I_{\min})/(I_{\max} + I_{\min})$ needs to be maximized. Apart from the aerial image, the practical resolution limit is determined by the availability of sensitive photoresists and the stability of the mask-wafer positioning system during exposure. Using an efficient illuminator, both throughput and imaging quality can be increased, which will also lead to higher resolution.[24] The aerial image is mainly defined by the transmission mask design and has a direct influence on the

achievable resolution. The analysis and optimization of the transmission masks regarding the achievable resolution require a deep understanding of the optical processes for the calculation of the resulting intensity distribution behind the mask. The achievable aerial image contrast not only depends on the mask material and geometry but also is a function of the grating period, especially for structure dimensions in the range of the utilized exposure wavelength. As analytical calculations are only valid if the half-pitch size is much larger than the exposure wavelength, for novel mask materials, rigorous simulation tools such as rigorous coupled-wave analysis (RCWA) need to be applied to display the complex intensity distribution behind the mask.

To achieve the highest possible contrast of the aerial image with achromatic Talbot lithography, phase-shifting transmission masks are most suitable. The mask geometry is designed to provide a π-phase shift for the radiation that passes through the grating material. If the mask geometry is designed precisely, this leads to a destructive interference between the radiation passing through the grating material and the gaps, respectively, and therefore to a cancellation of the 0'th diffraction order [see Fig. 1(b)]. In consequence, as the 0'th diffraction order contributes mainly to the background intensity $I_{\min}$ of the intensity distribution, a higher aerial image contrast can be achieved due to reduced background intensity. As the ± 1st diffraction orders dominate the interference pattern in this configuration, the complex interference pattern can be understood as a simple two-beam interference. To achieve a full compensation of the 0'th diffraction order, the beam part passing through the grating material must experience a precise π-phase shift, and the intensities of beam parts passing through the grating material and through the gaps need to be equal, taking the unavoidable absorption of EUV radiation in the grating material into account. This adds requirements on the precision and quality of both the mask design and the mask fabrication process.

3 Illumination Parameter Optimization

As the Talbot effect is based on interference, its effectiveness depends largely on the degree of temporal and spatial coherence of the utilized EUV radiation. To investigate the influence of coherence on the achievable aerial image contrast, an RCWA simulation model is used. For the simulations, the commercially available software Virtual Lab[25] with package 7.5.0 is used. The simulation parameters can be found in Table 1. For a resist-based phase-shifting mask as reported in Brose et al.[12] with line and space patterns of 80-, 40-, and 20-nm half-pitch (hp) (mask scale), the aerial image contrast at their respective achromatic Talbot distances is calculated depending on the relative spectral bandwidth $\Delta\lambda/\lambda$ [(0.1% to 20%, see Fig. 2(a)]. The spectral bandwidth is modeled by a set of incident plane waves of different wavelengths with intensities that are individually weighted according to a Lorentz distribution with a main wavelength of 13.5 nm and a full width at half maximum (FWHM) in accordance with the analyzed relative spectral bandwidth.

To analyze the aerial image contrast, cross-sections of the simulated two-dimensional intensity distribution behind the mask [see Fig. 1(a)] are taken at the achromatic Talbot distance, and the minimum intensity $I_{\min}$ and maximum intensity $I_{\max}$ are determined. The aerial image contrast is then calculated by $(I_{\max} - I_{\min})/(I_{\max} + I_{\min})$. As can be seen in Fig. 2, the aerial image contrast drops strongly with increasing relative spectral bandwidths. This effect can be explained by the deviation of the effective phase shift from π, as the optical parameters of the mask material differ for different wavelengths. As a small relative spectral bandwidth in the case of DPP EUV sources requires a strong spectral filtering and hence leads to a low amount of intensity in the

Table 1 Simulation parameters for the investigation of different illumination parameters.

	Temporal coherence			Spatial coherence		
Mask half-pitch (mask scale)	80 nm	40 nm	20 nm	80 nm	40 nm	20 nm
Main wavelength		13.5 nm			13.5 nm	
Relative spectral bandwidth		0.1% to 20%			4%	
Spatial coherence length		Infinite			1 to 100 μm	

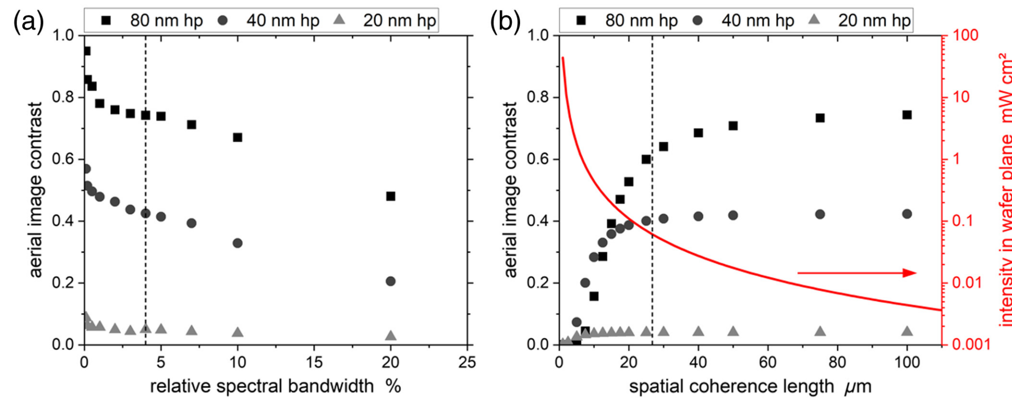

Fig. 2 Rigorous simulation analysis of the aerial image contrast for different relative spectral bandwidths (a) and spatial coherence lengths (b) for a line and space mask with mask half-pitches of 80, 40, and 20 nm (mask scale). The utilized temporal and spatial coherence of the experimental setup is indicated by a dotted black line.

mask plane, a spectral bandwidth of 2% to 5% should be preferred. The black dotted line refers to the utilized spectral bandwidth of 4%, as used in our experimental setup. As a minimal aerial image contrast that can still be resolved by state-of-the-art EUV photoresist, a value of 15 % is assumed on the basis of standard CMTF values. This means that for the analyzed mask design, a mask half-pitch of 20 nm cannot be printed onto the wafer, since the aerial image contrast is below 10 %.

To analyze the influence of the spatial coherence length, the same set of phase-shifting masks was simulated for a relative spectral bandwidth of 4% and a spatial coherence length from 1 to 100 μm [see Fig. 2(b)]. The spatial coherence length is modeled by a set of plane waves with different incidence angles θ with weighting factors that follow a Gaussian distribution with an FWHM given by $\theta_{\mathrm{FWHM}} = \arctan(\ln(2)\lambda/l_s\pi)$, where λ is the main wavelength and l_s is the spatial coherence length. The aerial image contrast at the achromatic Talbot distance increases strongly with the spatial coherence length for all investigated phase-shifting masks. Above a spatial coherence length of ∼50 μm, the aerial image contrast levels out. As the spatial coherence length in our setup can be increased only by the spatial filtering of the EUV beam, a large spatial coherence results in a low intensity in the wafer plane [see the right axis of Fig. 2(b)]. Therefore, a spatial coherence length of 20 to 40 μm should be used for exposures. The black dotted line indicates the currently used spatial coherence length of ∼25 μm as a reasonable trade-off between the intensity loss and the sufficient spatial coherence.

4 Simulative Mask Optimization

In the currently used mask design, an electron beam resist is used as the phase-shifting material. This allows for a simple and robust fabrication process[26] without the need for an additional etching transfer process. The phase shift and the resulting aerial image contrast in the wafer plane strongly depend on the mask geometry. The mask thickness can be precisely tuned by optimizing the spin coating and development process. For the gap/period ratio the electron beam lithography process has to be controlled, to enable the correct dose-to-size.[27] Following analytical calculations based on Schnopper et al.,[28] a π-phase shift is achieved for a mask thickness of 350 nm and a gap/period ratio of ∼0.4 for a wavelength of 13.5 nm. However, these calculations neglect the thickness-related effects of the mask and the effects that arise when the structure dimensions approach the wavelength, the effects called 3D mask effects. To optimize the aerial image contrast for different mask half-pitches, a rigorous simulation is therefore conducted for phase-shifting masks with half-pitches of 80, 40, and 20 nm (mask scale), considering a line and space structure geometry (see Fig. 3). The aerial image contrast is additionally multiplied by the transmission of the corresponding mask to ensure a mask geometry that is usable for an exposure with the limited EUV intensity provided by the DPP EUV source. This transmission-weighted aerial image contrast at achromatic Talbot distance is calculated for irradiation with a 13.5-nm main

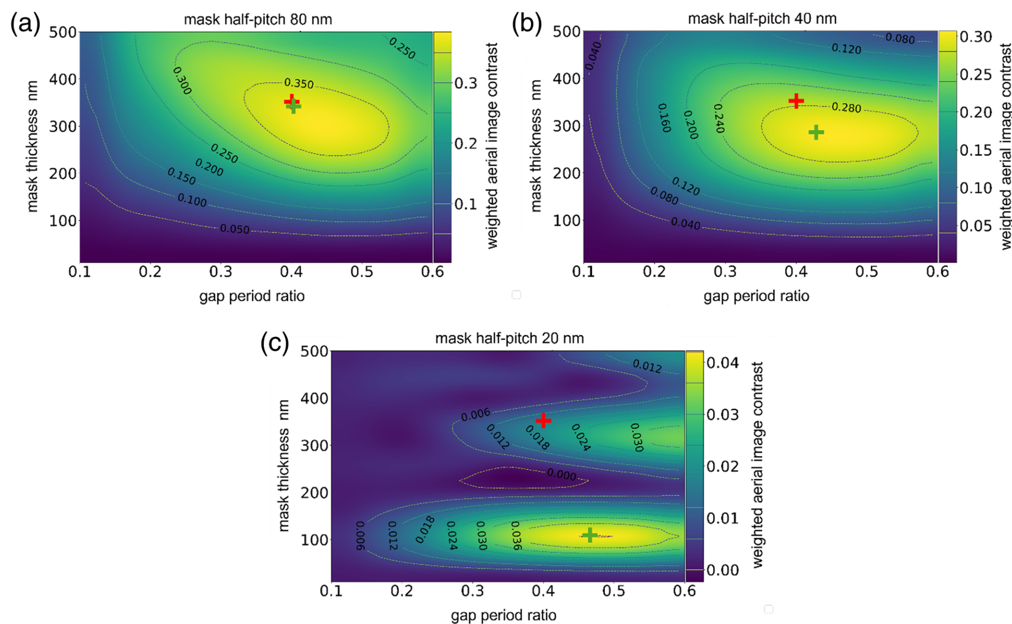

Fig. 3 Rigorous simulation analysis of the aerial image contrast for different mask thickness gap/period ratios and mask half-pitches of 80, 40, and 20 nm (mask scale). The analytical mask thickness is indicated by a red cross. The rigorously optimized mask geometry is indicated by a green cross. It is in good agreement with the analytical result for a mask half-pitch of 80 nm but differs strongly for 40- and 20-nm half-pitch. In addition, the achievable transmission-weighted aerial image contrast decreases from ~0.38 for the 80-nm half-pitch to ~0.04 for the 20-nm half-pitch (mask scale).[29]

wavelength and a relative spectral bandwidth of 4%. For each mask half-pitch, the mask thickness is varied from 10 to 500 nm, and the gap/period ratio is varied from 0.1 to 0.6. The analytically optimized geometry based on Schnopper et al.[28] is marked by a red cross. For a mask half-pitch of 80 nm (mask scale), the rigorously optimized geometry is in good agreement with the analytical result. The maximum weighted aerial image contrast is 0.38, close to the analytical calculation. In addition, the simulation shows a large area of geometrical parameters that still allow for a high aerial image contrast. For the 40-nm half-pitch (mask scale), the weighted aerial image contrast decreases to a maximum of 0.31, and the optimal mask geometry deviates stronger from the analytical result because the relation $d \gg \lambda$ does not hold true anymore.[30] The maximal weighted aerial image contrast is achieved for a mask thickness of ~270 nm and a gap/period ratio of 0.43. This deviation gets even stronger for a 20-nm half-pitch (mask scale), where the maximal weighted aerial image contrast is achieved for a mask thickness of ~115 nm and a gap/period ratio of 0.48. However, the weighted aerial image contrast does not exceed 0.05 for this mask half-pitch.

To observe the decrease in aerial image contrast with decreasing mask half-pitch more precisely, the rigorous optimization of the aerial image contrast is performed for mask half-pitches from 5 to 80 nm (mask scale, see Fig. 4). For each mask half-pitch, the highest achievable aerial image contrast is plotted by optimizing the mask material thickness and the aspect ratio for each half-pitch. The aerial image contrast drops from ~75% for the 80-nm mask half-pitch to ~50% for the 40-nm mask half-pitch to below 10% for the 20-nm half-pitch (mask scale). To evaluate the resulting resolution limit for resist patterning, the CMTF of the utilized photoresist needs to be considered.[31,32] This parameter describes the minimal aerial image contrast required to transfer the aerial image into a resist topography for a resist with given sensitivity and contrast. If an industrial EUV photoresist with CMTF of 15% is used, a mask pattern with a half-pitch of 28 nm (mask scale) would still lead to a sufficient aerial image contrast for pattern transfer. Due to the achromatic Talbot effect, the realized pattern on the wafer will be demagnified to ~14-nm half-pitch (wafer scale). It has to be noted however, that additional process imperfections often lead to a higher required CMTF and this calculation can therefore be understood as the

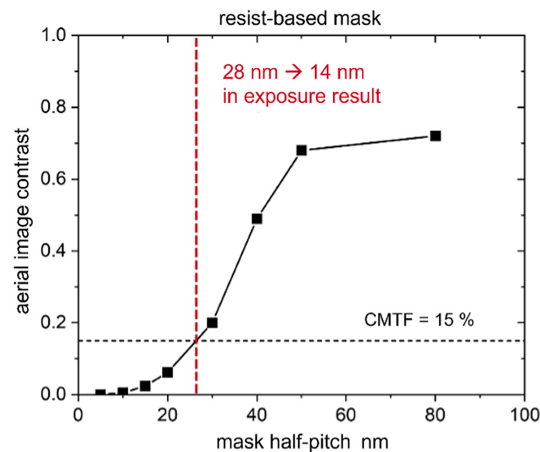

Fig. 4 Rigorous simulation results for the aerial image for different mask half-pitches of a resist-based transmission mask. For each mask half-pitch, the mask geometry was optimized using rigorous simulations analogous to Fig. 3. For an EUV photoresist with CMTF 15%, the resolution limit is at 28-nm mask half-pitch (mask scale), which would lead to 14 nm in the exposure result (wafer scale) due to the achromatic Talbot demagnification.

theoretical limit. Additionally, it is evident that the resist-based mask design has limitations towards the target resolution of sub-10 nm half-pitch (wafer scale), which would be necessary for resist qualification for future technology nodes. Therefore, alternative mask materials are investigated.

For the evaluation of materials with suitable optical properties, the tabulated complex refractive indices (n and k) of possible mask materials are considered.[33] The maximum achievable aerial image contrast multiplied by the transmission is calculated for these refractive indices via an optimization algorithm under the analytical premise that the grating size is significantly larger than the irradiation wavelength. In Fig. 5, the parameter space from 0.91 to 1 for n and from 0 to 0.031 for k is shown with the according material values indicated by a blue dot. The maximum achievable aerial image contrast multiplied by transmission for every parameter combination is indicated by a color following a color bar ranging from 0 to 1. Several metallic materials and material combinations can be identified for further analysis (indicated by a white dotted frame).

In earlier investigations, a molybdenum nitride (MoN) based mask was shown to exhibit the highest aerial image contrast[19] and good patterning performance in etching processes.[9] Therefore, the rigorous analysis shown above for the resist-based mask is repeated for an MoN-based line and space transmissions mask with mask half-pitches of 40, 20, and 10 nm

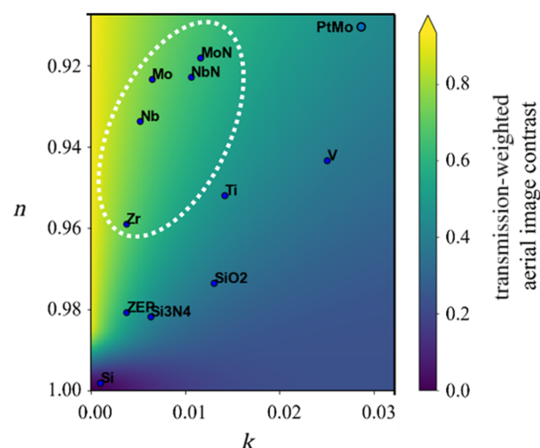

Fig. 5 Analytical optimization of the aerial image contrast multiplied by transmission for combinations of n (from 0.91 to 1.00) and k (from 0.00 to 0.033). Selected materials and material combinations are marked, and suitable materials are indicated by the white dotted frame.

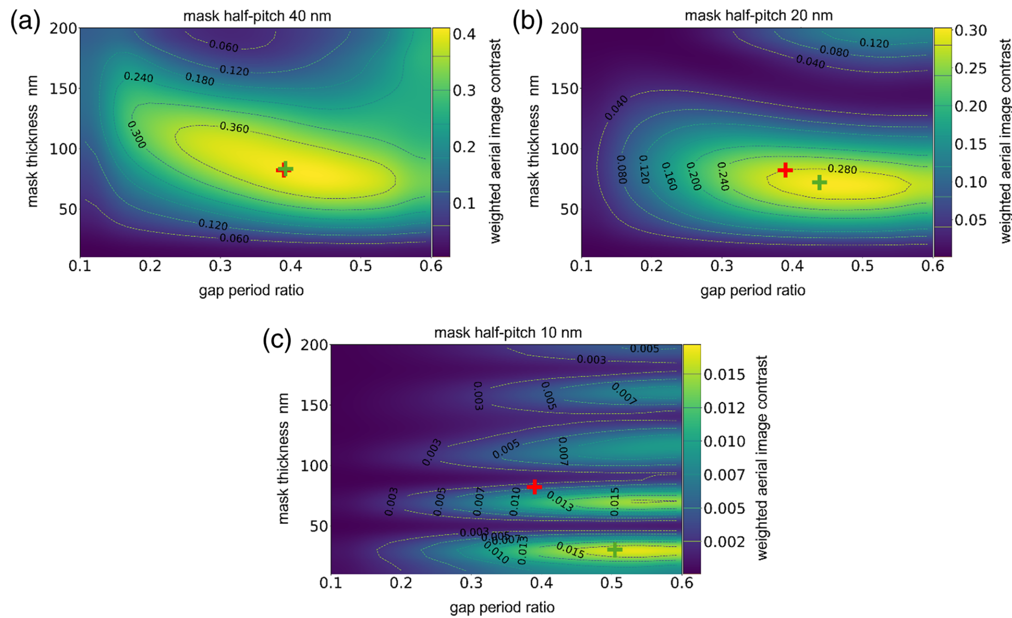

Fig. 6 Rigorous simulation analysis of the aerial image contrast for different mask thickness gap/period ratios and mask half-pitches of 40, 20, and 10 nm (mask scale). The analytical mask thickness is indicated by a red cross. The rigorously optimized mask geometry is indicated by a green cross. It is in good agreement with the analytical result for a mask half-pitch of 40 nm but differs strongly for 20- and 10-nm half-pitch. In addition, the achievable transmission-weighted aerial image contrast decreases from ∼0.41 for the 40-nm half-pitch to ∼0.015 for the 10-nm half-pitch.[29]

(mask scale, see Fig. 6). The qualitative behavior of the aerial image contrast is the same as for the resist-based mask. However, using the MoN-based mask exhibits certain advantages. The weighted aerial image contrast is above 30% for mask half-pitches down to 20 nm (mask scale). In addition, the rigorously optimized mask geometry does not deviate strongly from the analytical mask design. For the 10-nm half-pitch (mask scale), the weighted aerial image contrast drops down to below 2%, and the rigorously optimized mask geometry shows strong deviations from the analytical result.

To identify the resolution limit for the MoN-based mask, the maximal aerial image contrast is compared for mask half-pitches from 5 to 80 nm (mask scale, see Fig. 7). The mask geometry was optimized for each individual mask half-pitch to exhibit the highest transmission-weighted

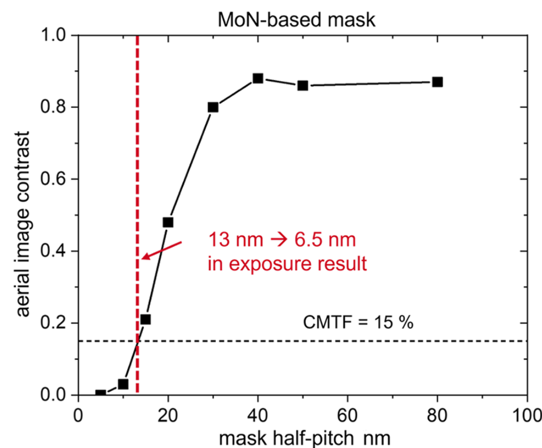

Fig. 7 Rigorous simulation results for the aerial image for different mask half-pitches of a MoN-based transmission mask. For each mask half-pitch, the mask geometry was optimized using rigorous simulations analogous to Fig. 6. For an EUV photoresist with CMTF 15%, the resolution limit is at 13-nm mask half-pitch (mask scale), which will lead to 6.5 nm in the exposure result (wafer scale) due to the achromatic Talbot effect.

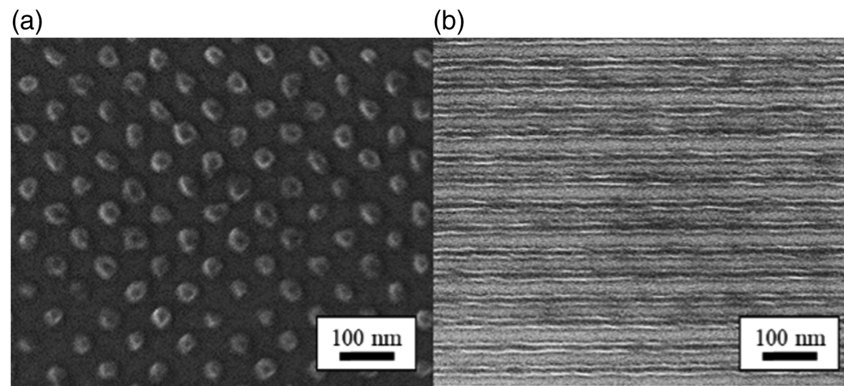

Fig. 8 Scanning electron microscopy (SEM) images of the achievable patterning results for pinhole patterns (a) and lines and spaces (b) for a mask thickness of 270 nm, printed in a standard EUV photoresist with the current resist-based phase-shifting mask design. Pinhole patterns with a 28-nm hp and line patterns with a 32.5-nm hp (wafer scale) are shown.

aerial image contrast. The aerial image contrast is above 80% for mask half-pitches down to 30 nm (mask scale) and then decreases strongly. If an average EUV photoresist with CMTF of 15% is assumed, a mask pattern with a half-pitch of 13 nm (mask scale) would still have a sufficient aerial image contrast for pattern transfer. Due to the achromatic Talbot effect, the realized pattern on the wafer would be demagnified to ∼6.5-nm half-pitch (wafer scale). For a mask half-pitch of 20 nm that leads to a resolution of 10-nm half-pitch in the exposure result (wafer scale), the aerial image contrast is still ∼50%. The MoN-based mask would therefore suffice to reach the targeted sub-10-nm resolution (wafer scale) for resist qualification for current and future technology nodes.

5 Experimental Exposure Results

In addition to the simulative optimization of the phase-shifting transmission mask, the mask fabrication feasibility must be considered in the development of a mask design. The current mask fabrication process is based on an electron beam resist mask that can be directly patterned on top of a 25-nm SiN_x membrane window and is described in previous publications.[26,34] The relatively simple fabrication process leads to several advantages such as the fast optimization and testing of different mask designs. However, as the required mask thickness for the targeted π-phase shift can be calculated to 350 nm for the utilized resist,[28] several disadvantages of the fabrication process need to be considered. For every smaller mask feature, the aspect ratio (ratio of mask thickness to structure dimension) increases rapidly, which leads to increasing pattern instability, especially for line structures.[34] This can be explained by increased capillary forces during the evaporation of the development stopper and by the stronger influence of the membrane curvature during vacuum-chucking, especially for higher aspect ratios. In addition, an increasing thickness loss of the resist can be observed for denser structures, leading to further deviations from the target grating design.

Several transmission masks with different mask thicknesses were fabricated and tested in the compact EUV exposure tool. For a 270-nm mask thickness, patterns down to a 28-nm hp for pinhole patterns and a 32.5-nm hp for lines and spaces (wafer scale) could be demonstrated in a standard EUV photoresist, which is to the best of our knowledge the current record resolution for Talbot lithography with laboratory-based EUV nanopatterning setups (see Fig. 8). The high line edge roughness for the lines and spaces pattern [see Fig. 8(b)] is most likely originating from the utilized EUV photoresist, since roughness or defects in the mask pattern will be compensated by the interference effect.[35]

6 Conclusion and Outlook

In this contribution, the authors present the simulative and experimental investigation of the influencing factors on the resolution limit of Talbot lithography with compact exposure tools.

The influence of spatial and temporal coherence of the utilized radiation on the achievable resolution is investigated by rigorous wave optical simulations. Reduced spatial and temporal coherence leads to decreased aerial image contrast, but increasing the coherence is accompanied by radiation losses. Therefore, these illumination parameters need to be carefully selected. The main challenge for the advancement of Talbot lithography with EUV radiation is the mask fabrication. To enable the required phase-shift of the EUV radiation passing through the mask, a high thickness of the mask material relative to the mask pitch is needed, leading to challenges in both fabrication and imaging. The influence of the geometry and utilized material of the phase-shifting transmission masks is therefore investigated both by rigorous wave-optical simulation and experimental exposure of standard EUV photoresists. Several influencing factors on the achievable resolution are determined and characterized. Periodic pinholes and line patterns are created with sub-30 nm resolution (wafer scale). To move further towards sub-10 nm resolution (wafer scale) for future technology nodes, metallic phase-shifting masks are considered and characterized by rigorous simulations and several suitable materials are identified, paving the way to high-resolution periodic patterns.

Disclosures

The authors declare no conflicts of interest.

Code and Data Availability

Data underlying the results presented in this paper are available in Henke et al.[33]

Acknowledgments

The authors would like to thank the cleanroom staff of the Helmholtz Nanoelectronic Facility at Research Center Jülich, Germany.[36] This work was realized by cooperation activities in the frame of the Jülich Aachen Research Alliance for Fundamentals of Future Information Technology (JARA-FIT). The presented activities received funding from the German Research Foundation (DFG; Support Code: DA 990/4-1).

References

1. D. de Simone, Y. Vesters, and G. Vandenberghe, "Photoresists in extreme ultraviolet lithography (EUVL)," *Adv. Opt. Technol.* **6**(3–4), 163–172 (2017).
2. P. Naulleau et al., "EUV resists: pushing to the extreme," *J. Photopolym. Sci. Technol.* **27**(6), 725–730 (2014).
3. A. Banerjee, S. Maity, and C. H. Mastrangelo, "Nanostructures for biosensing, with a brief overview on cancer detection, IoT, and the role of machine learning in smart biosensors," *Sensors* **21**(4), 1253 (2021).
4. J. Tempeler et al., "Structural properties of templated Ge quantum dot arrays: impact of growth and prepattern parameters," *Nanotechnology* **29**(27), 275601 (2018).
5. K. Bi et al., "All-dielectric metamaterial fabrication techniques," *Adv. Opt. Mater.* **9**(1), 2001474 (2021).
6. A.-M. Goethals et al., "EUV resist process performance investigations on the NXE3100 full field scanner," *J. Photopolym. Sci. Technol.* **25**(5), 559–567 (2012).
7. D. Kazazis, L. Tseng, and Y. Ekinci, "Improving the resolution and throughput of achromatic Talbot lithography," *J. Vac. Sci. Technol. B* **36**, 06J501 (2018).
8. T. Watanabe and T. Harada, "Research activities of extreme ultraviolet lithography at the University of Hyogo," *Sync. Rad. News* **32**(4), 28–35 (2019).
9. D. Fan and Y. Ekinci, "Photolithography reaches 6 nm half-pitch using EUV light," *Proc. SPIE* **9776**, 97761V (2016).
10. Z. Tasdemir et al., "Chemically amplified EUV resists approaching 11 nm half-pitch," *Proc. SPIE* **10583**, 105831W (2018).
11. K. Bergmann, S. V. Danylyuk, and L. Juschkin, "Optimization of a gas discharge plasma source for extreme ultraviolet interference lithography at a wavelength of 11 nm," *J. Appl. Phys.* **106**, 073309 (2009).
12. S. Brose et al., "Achromatic Talbot lithography with partially coherent extreme ultraviolet radiation: process window analysis," *J. Micro/Nanolith. MEMS MOEMS* **15**(4), 043502 (2016).
13. S. Yang et al., "Influence of symmetry and duty cycles on the pattern generation in achromatic Talbot lithography," *J. Vac. Sci. Technol. B* **35**, 021601 (2017).
14. A. Isoyan et al., "Talbot lithography: self-imaging of complex structures," *J. Vac. Sci. Technol. B* **27**(6), 2931–2937 (2009).

15. T. Sato et al., "Printability of defects in Talbot lithography," *Microelectron. Eng.* **143**, 21–24 (2015).
16. A. Lohmann and J. Thomas, "Making an array illuminator based on the Talbot effect," *Appl. Opt.* **29**, 4337–4340 (1990).
17. H. H. Solak and Y. Ekinci, "Achromatic spatial frequency multiplication: a method for production of nanometer-scale periodic structures," *J. Vac. Sci. Technol. B* **23**(6), 2705–2710 (2005).
18. H. Talbot, "Facts relating to optical science," *London Edinburgh Dublin Philos. Mag. J. Sci.* **9**(56), 401–407 (1836).
19. F. Lord Rayleigh, "On copying diffraction gratings and on some phenomenon connected therewith," *London Edinburgh Dublin Philos. Mag. J. Sci.* **11**(67), 196–205 (1881).
20. B. Lüttgenau et al., "Design and realization of an in-lab EUV dual beamline for industrial and scientific applications," *Proc. SPIE* **11854**, 1185419 (2021).
21. L. Rayleigh, "XXV. On copying diffraction-gratings, and on some phenomena connected therewith," *London Edinburgh Dublin Philos. Mag. J. Sci.* **11**(67), 196–205 (1881).
22. J. Vieker and K. Bergmann, "Influence of the electrode wear on the EUV generation of a discharge based extreme ultraviolet light source," *J. Phys. D: Appl. Phys.* **50**, 345601 (2017).
23. S. Brose et al., "EUV-LET 2.0: a compact exposure tool for industrial research at a wavelength of 13.5 nm," *Proc. SPIE* **10957**, 109571K (2019).
24. B. Lüttgenau et al., "Design of an efficient illuminator for partially coherent sources in the extreme ultraviolet," *Appl. Opt.* **61**(11), 3026–3033 (2022).
25. VirtualLab Fusion 7.5.0, "LightTrans GmbH," https://www.lighttrans.com (valid by 2024).
26. S. Brose et al., "Optimized phase-shifting masks for high-resolution resist patterning by interference lithography," *Proc. SPIE* **10450**, 104502A (2017).
27. B. Lüttgenau et al., "Design and realization of an industrial stand-alone EUV resist qualification setup," *Proc. SPIE* **11517**, 115171F (2020).
28. H. W. Schnopper et al., "Diffraction grating transmission efficiencies for XUV and soft x-rays," *Appl. Opt.* **16**, 1088 (1977).
29. B. Lüttgenau et al., "Investigation of the resolution limit of Talbot lithography with compact EUV exposure tools," *Proc. SPIE* **12802**, 1280203 (2023).
30. D. Gremaux and N. Gallagher, "Limits of scalar diffraction theory for conducting gratings," *Appl. Opt.* **32**(11), 1948–1953 (1993).
31. M. J. Bowden et al., "The physics and chemistry of the lithographic process," *J. Electrochem. Soc.: Rev. News* **128**, 195–214 (1981).
32. R. W. Wake et al., "A review of contrast in positive photoresists," *Proc. SPIE* **0539**, 291–298 (1985).
33. B. L. Henke, E. M. Gullikson, and J. C. Davis, "X-ray interactions: photoabsorption, scattering, transmission, and reflection at E D 50-30,000 eV, Z D 1-92," *At. Data Nucl. Data Tables* **54**, 181–342 (1993).
34. B. Lüttgenau et al., "Toward the resolution limit of Talbot lithography with compact EUV exposure tools," *Proc. SPIE* **12292**, 1229208 (2022).
35. T. Allenet and I. Mochi, "EUV interference lithography: impact of mask roughness on feature patterning," *Proc. SPIE* **PC12292**, PC1229207 (2022).
36. Forschungszentrum Jülich GmbH, "HNF—Helmholtz Nano Facility," *J. Large-Scale Res. Facilities* **3**, A112 (2017).
37. B. Lüttgenau et al., "Novel high-contrast phase-shifting masks for EUV interference lithography," *Proc. SPIE* **11323**, 113231Q (2020).

Bernhard Lüttgenau is a postdoctoral scholar at the Lawrence Berkeley National Lab. He received his doctoral degree in 2024 from RWTH Aachen University, Germany, where he conducted research on EUV interference lithography employing partially coherent EUV sources. His current research focuses on the fundamental characterization of EUV resist materials using advanced spectroscopic techniques with EUV and soft X-ray radiation. He has authored or co-authored more than 10 journal and proceedings papers.

Sascha Brose graduated in mechanical engineering in 2008 and received his PhD in mechanical engineering in 2019 from RWTH Aachen University. Currently, he is the group manager of the research group EUV Technology at the Chair for Technology of Optical Systems at the RWTH Aachen University. He has authored or co-authored 40 scientific publications mainly in the field of EUV lithography and metrology.

Biographies of the other authors are not available.